Bellymount-Pulsed Tracking: A Novel Approach for Real-Time In vivo Imaging of *Drosophila* Oogenesis

Shruthi Balachandra[1] and Amanda A. Amodeo[1]

Department of Biological Sciences, Dartmouth College, Hanover, New Hampshire, USA

email: shruthi.balachandra@dartmouth.edu, amanda.amodeo@dartmouth.edu.

ABSTRACT

Quantitative live imaging is a valuable tool that offers insights into cellular dynamics. However, many fundamental biological processes are incompatible with current live imaging modalities. *Drosophila* oogenesis is a well-studied system that has provided molecular insights into a range of cellular and developmental processes. The length of the oogenesis coupled with the requirement for inputs from multiple tissues has made long-term culture challenging. Here, we have developed Bellymount-Pulsed Tracking (Bellymount-PT), which allows continuous, non-invasive live imaging of *Drosophila* oogenesis inside the female abdomen for up to 16 hours. Bellymount-PT improves upon the existing Bellymount technique by adding pulsed anesthesia with periods of feeding that support the long-term survival of females during imaging. Using Bellymount-PT we measure key events of oogenesis including egg chamber growth, yolk uptake, and transfer of specific proteins to the oocyte during nurse cell dumping with high spatiotemporal precision within the abdomen of a live female.

KEYWORDS: oogenesis, in vivo live imaging, developmental dynamics, protein accumulation

SUMMARY STATEMENT

Bellymount-Pulsed Tracking is a novel tool to capture in vivo dynamics of for long periods in *Drosophila* oogenesis.

INTRODUCTION

Advances in live imaging have been essential for unraveling the dynamics of key molecular events during a variety of biological processes. However, not all processes are equally amenable to live imaging. Capturing very small or rapid molecular events requires sophisticated microscopy (Fuhrmann et al., 2022). Conversely, processes occurring over longer timescales such as growth and development require preserving tissue health during long-term imaging (Martin et al., 2018; Morris and Spradling, 2011; Peters and Berg, 2016; Tsao et al., 2016). *Drosophila* oogenesis is one process that has proven to be resistant to long-term live imaging despite a wealth of genetic tools and molecular characterization (King, 1970; Spradling, 1993; Shimada et al., 2011; Lebo and McCall, 2021; Morris and Lehmann, 1999; Avilés-Pagán et al., 2020; Imran Alsous et al., 2021; Jackson et al., 2023). The major challenge in capturing the journey from a germline stem cell (GSC) to a fertilizable egg is that the process lasts about 7 days and happens inside the female abdomen (He et al., 2011). The GSCs reside in the germarium at the anterior tip of the ovary. Differentiating cells leave the stem cell niche and undergo 4 rounds of incomplete mitosis to generate a 16-cell cyst. One cell is specified as the oocyte and the rest become nurse cells which will endocycle to produce the bulk of the materials required for oocyte growth. The 16 germline cells are encapsulated by a layer of somatic follicle cells to form an egg chamber. The egg chamber exists the germarium and grows several orders of magnitude in volume while undergoing a stereotyped procession of developmental milestones over a period of about 3 days (Dapples and King, 1970; King, 1970; He et al., 2011; Diegmiller et al., 2021). The developing egg chambers migrate posteriorly down the length of the ovary following one another in an assembly line called an ovariole. Each ovariole contains 5-7 egg chambers at any given time and a pair of ovaries will have 32-45 ovarioles (David and Merle, 1968; King, 1970) .

Historically, most studies of *Drosophila* oogenesis have been performed using fixed samples which necessarily limit the ability to resolve dynamic processes (King, 1970; Spradling, 1993; Diegmiller et al., 2021; Imran Alsous et al., 2021; Weichselberger et al., 2022). However, as early as the 1970s efforts have been made to develop ex-vivo culture protocols for late-stage egg chambers (Petri et al., 1979; Gutzeit and Koppa, 1982). Optimization of late-stage cultures allows survival of stage 10-14 egg chambers for up to 10 hours (Peters and Berg, 2016; Parsons et al., 2023; Zhang and Liu, 2024). Stage 9 and earlier egg chambers have proven to be more difficult to culture and require the addition of insulin to the media to achieve survival for 4-5 hours (Prasad and Montell, 2007). Further refinement of the culture media allowed for the survival of the germarium to a maximum of 13 hours with follicle cell division rates declining after 6-8 hours (Morris and Spradling, 2011). Nevertheless, the specific growth rates in these culture conditions have not been reported and to date, many live-imaging studies are limited to only a few hours before egg chambers stall their growth and begin dying (Inaki et al., 2022; Zajac et al., 2023). Collectively, these

techniques allow a short window to observe processes including the germline-soma coordination in the germarium (Morris and Spradling, 2011; Wilcockson and Ashe, 2021), shuttling of biomolecules across the egg chamber (Shimada et al., 2011; Lu and Gelfand, 2022), follicle cell morphology and migration (Prasad and Montell, 2007; Haigo and Bilder, 2011; Lei et al., 2023; Williams et al., 2022; Miao et al., 2022; Jackson et al., 2023a), and nurse cell changes during later stages of oogenesis (Yalonetskaya et al., 2020; Imran Alsous et al., 2021; Jackson et al., 2023a). Recently, Marchetti et al developed a revolutionary multi-organ co-culture system that successfully maintains egg chamber integrity for up to 3-4 days. However, growth rates remain substantially lower than in vivo and egg chambers fail to progress through developmental landmarks at the appropriate pace(Marchetti et al., 2022)

The recently developed Bellymount tool by Koyama et al (2020) allows visualization of the internal organs including the midgut, crop, and ovaries without the need to open the fly's abdomen by affixing the fly between two glass coverslips using transparent, nontoxic Elmer's glue. In the original protocol flies were imaged over several days and were released from the mount in between image acquisitions. Though this technique captures unperturbed cellular dynamics in vivo with unprecedented resolution, the need to repeatedly capture and re-mount flies prevents tracking in tissues that lack morphological guideposts for image alignment. This is particularly problematic for oogenesis since each female has dozens of egg chambers, each growing rapidly and moving posteriorly during developments. To overcome this challenge, we developed Bellymount-Pulsed Tracking (Bellymount-PT) by combining the original Bellymount restraint with pulsed anesthesia, and a liquid diet to allow long-term imaging and tracking of developing egg chambers for periods up to 12-16 hours. The prolonged imaging duration enabled us to track egg chamber growth and visualize their transition between developmental stages. Further, we were able to quantify aspects of yolk uptake and histone accumulation during nurse cell dumping, which have never been previously observed in an in vivo system. This study provides a novel technique for generating insight into the key events of oogenesis in an in vivo system with minimal experimental perturbation.

RESULTS AND DISCUSSION

Bellymount - Pulsed Tracking integrates image acquisition with anesthesia to allow long-term imaging in the mount

To maintain long-term tissue health in the endogenous physiological context for egg chamber growth we developed Bellymount-PT. Flies were secured between two glass coverslips, the bottom of which was a 50 mm MatTek dish using Elmer's glue and 0.48 mm adhesive spacers (Fig. 1A). Flies were repeatedly anesthetized using CO_2 to prevent voluntary and involuntary movements during image acquisition, and allowed to awaken and feed between timepoints (Poinapen et al., 2017; Koyama et al., 2020; Tang et al.,

2021). Since CO_2 anesthesia adversely affects fertility in flies (Shen et al., 2020) we minimized the duration of anesthesia by integrating image acquisition with CO_2 pulsing via an Arduino controller. The Arduino opened a solenoid valve on the CO_2 tank in response to a signal from the image acquisition software (Fig. 1B) 2 minutes before the beginning of imaging and closed the valve immediately after image acquisition. Pulsed anesthesia allowed flies to feed, defecate, and lay eggs while restrained in the mount (Fig. 1A,C,D). We tracked egg chambers with imaging intervals from 10 min to 2 hours depending on the experimental requirements.

Up to 5 flies can be mounted on a single 50 mm dish (Fig. 1B,D; Movie 2). We typically imaged 3-4 flies during each session and the unimaged flies served as controls to determine the effects of laser exposure on fly health (Fig.2A,B). This ability to image multiple flies in a single experiment will help to control for day-to-day variability when multiple genotypes are imaged simultaneously. Since oogenesis is extremely sensitive to the nutritional status of the female (Terashima and Bownes, 2004; Shimada et al., 2011), we developed a custom apple juice and yeast extract liquid food which was provided via a cotton wick in a bent capillary feeder tube (Fig.1A, S1). To stimulate olfactory feeding cues, we included fresh yeast paste and banana baby food within the reach of each fly's legs. The food and a moist absorbent pad positioned at the top of the imaging chamber kept the flies hydrated during imaging (Fig. 1A-D).

Females mounted for Bellymount-PT remain alive and fecund

Limiting the exposure to anesthesia to once every 2 hours and providing continuous access to food allowed ~60% flies to survive for greater than 16 hours of imaging (Fig. 2A). To understand the causes of mortality during imaging we maintained controls on standard food in vials, in the mount without exposure to CO_2 or laser, and on the microscope exposed to repeated anesthesia but not imaged. As expected, nearly all flies maintained in vials survived and flies restrained in the mount and exposed to both laser and CO_2 had the highest mortality. The bulk of the mortality seems to be due to the restraint system itself since the flies in the mount that were not exposed to anesthesia or the laser had only about a 10% increase in survival compared to those that were imaged. We observed that much of the mortality resulted from drowning or dehydration when the wick for the liquid food was not ideally placed above the fly.

Fecundity is a crude reflection of the rate of egg chamber development. To understand the influence of experimental conditions on egg production, we counted the eggs laid by females imaged during an overnight (16 hour) session, along with other controls as described above. Restrained flies frequently continued to lay eggs which accumulated in the mount at the posterior of the fly (Fig. 1C, Movie1-3). On average, flies that remained in their food vials at 19-20°C laid 10±2 (SEM) (n=37), while flies that were

137 imaged laid 3±1 (SEM) eggs per female overnight (n=59) (Fig.2B). Although restraint did significantly
138 reduce egg production (p<0.0001), the fact that egg production continues even during imaging indicates
139 that oogenesis is not completely stalled under the Bellymount-PT protocol.
140
141 **Imaging through the cuticle allows single-cell resolution of developing egg chambers**
142 Bellymount-PT allows the identification of all stages of oogenesis from the germarium through stage 14
143 using H2Av-mRFP, although not all stages were visible in the same female (Fig. 1E-G). We were able to
144 resolve individual H2Av-mRFP nuclei and Moesin-GFP at the cortex within egg chambers to a Z-depth of
145 75-80 µm using an Olympus multiphoton microscope with a 25x water objective (NA 1.05) (Fig.2C). The
146 nuclear signal of follicle cells defined the outer egg chamber boundary allowing for accurate three-
147 dimensional reconstruction of full egg chamber volumes up to stage 8 (stage 6 shown in the Fig. 2D). Later-
148 stage egg chambers could not be imaged to their full depth, but in all cases, the midsection area functions
149 as a proxy for egg chamber size. We could resolve subcellular structures including ring canals and oocyte
150 chromatin (Fig. 2C-E'; Movie 4-6). At lower magnification (Zeiss 980 with a 10x NA0.5 air objective)
151 several egg chambers of different ages can be imaged simultaneously, (Fig. 2G) increasing the throughput
152 of the technique. The wider range of view of the lower magnification objective also aided in long-term
153 tracking since egg chambers move within the female abdomen throughout development and the female
154 herself moves a small amount within the restraints during imaging intervals. Under these conditions, we
155 can track multiple egg chambers through different stages of development for 8-16 hours (stage 10-14,
156 Fig.2G,H, Movie 7,8; stage 7-8, Fig.3F, Movie 9).
157
158 **Bellymount-PT enables tracking live growth rates of individual egg chambers**
159 Due to the challenges of live imaging oogenesis, existing estimates of egg chamber growth rates are based
160 on the number of egg chambers of each stage in individual females at a given time and the average number
161 of eggs laid per female per day. Moreover, literature estimates differ greatly in the time assigned to each
162 stage due to differences in genetic backgrounds and fly husbandry (David and Merle, 1968; King, 1970;
163 Spradling, 1993). To account for our own strains and fly husbandry, we generated a new growth curve for
164 the developmental time of w; Mat-α-tub67-gal4/CyO; Mat-α-tub15-gal4, H2Av-mRFP/TM3 females
165 maintained at 23±1°C. Note that our standard growth curve is constructed from flies that were kept at
166 warmer temperatures than our imaging conditions. Since the conventional staging of egg chambers is
167 largely based on size and we wanted to measure growth rates, we staged the egg chambers based on size-
168 independent parameters whenever possible and measured the egg chamber midsection area for each stage
169 from the fixed samples (n=15 females; n=234 egg chambers) (Fig. 3A; see methods). We recorded the
170 fecundity (eggs laid/female/day=52±2.7 SEM), egg production rate (1.45 eggs/per ovariole/day), and the

171 frequency of each stage in an ovariole to estimate the duration of each stages 2-14 (Table S1). This data
172 allowed us to estimate the expected growth rate for egg chambers during unperturbed oogenesis which is
173 well fit by an exponential equation ($A=273\ e^{0.06t}$, where t=time in hours and A=area in μm^2). Our measured
174 standard growth curve is within the range reported in previous literature (King, 1970; Spradling, 1993)
175 (Fig.3B).
176
177 Next, we sought to measure the real-time growth rate of individual egg chambers inside the female abdomen
178 using Bellymount-PT. We were able to track the growth of egg chambers which were initially in stages 4-
179 10. We measured the midsection area of each egg chamber over time. To test if the growth rates observed
180 using Bellymount-PT matched those expected from the fixed growth curve we aligned each trace to the
181 growth curve based on the initial area with the subsequent times based on the imaging intervals. While
182 some egg chambers had growth rates that aligned well with the expected growth curves (Fig. 3C-G, Movie
183 9), most grew more slowly than our standard (Fig. 3C-E, H,I, Movie 10). During the initial 2 hours of
184 imaging, the imaged egg chambers reached an average of 90% of the expected size, however by 8 hours,
185 they had only reached 75% (Fig. S2). We note that although growth rates decreased, many of the size-
186 independent aspects of oogenesis progressed at a relatively normal rate indicating that the egg chambers
187 continued to develop. This suggests that the midsection area may be an underestimate of egg chamber
188 volume when the egg chambers remain within the female abdomen compared to fix samples compressed
189 between two coverslips. In particular, stage 10 egg chambers were often seen to progress to stage 14 in
190 about 10 hours as expected but did not appear to grow as much as expected (Fig.2 GH).
191
192 **Bellymount-PT allows unprecedented visualization of the events of oogenesis**
193 Finally, we employed Bellymount-PT to capture dynamic protein localization events during oogenesis.
194 First, we focused on the uptake of yolk protein into the oocyte from the hemolymph. The initiation of yolk
195 uptake is a checkpoint for further progression of the egg chamber development. Active yolk uptake starts
196 from early stage 8 and continues through stage 10 (Terashima and Bownes, 2004; Shimada et al., 2011;
197 Row et al., 2021; Isasti-Sanchez et al., 2021). Inadequate nutrition and environmental stress stall oogenesis
198 at stages 7 or early 8 by preventing yolk uptake (Terashima and Bownes, 2004; Shimada et al., 2011; Hara
199 and Yamamoto, 2022). *Drosophila* yolk proteins (Yp1-3) are predominantly made in fat bodies and ovarian
200 follicle cells, and their endocytosis by the oocyte is stimulated by factors including hormonal levels
201 (Richard et al., 1998) and male-derived sex peptide received during mating (Soller et al., 2006). Thus, yolk
202 accumulation requires the coordination of multiple organ systems and external factors. This explains the
203 difficulty in maintaining egg chamber growth during these active vitellogenic stages in ex vivo culture
204 systems (Peters and Berg, 2016). To test if Bellymount-PT supports yolk uptake, we tracked Yp1:GFP

205 (Hara and Yamamoto, 2022) accumulation in a stage 8-10 egg chambers (n=6). Since in later stages growth
206 is dependent on yolk uptake, we aligned the growth curves to the expected initial age based on the initial
207 oocyte percentage instead of the midsection area (Fig. 4C). We used an endogenously tagged H2Av-
208 mCherry to manually segment the oocyte and measured the total amount of Yp1-GFP protein in ½ of the
209 egg chambers over time. We found that yolk continually accumulates at a relatively constant rate for the
210 duration of the measured stages (Fig. 4A,B, Movie 11). These measurements of yolk uptake from the
211 hemolymph are only possible by preserving the physiological context inside the intact female abdomen
212 using Bellymount-PT.
213
214 Finally, we were interested in measuring maternal protein transfer from the neighboring nurse cells to the
215 oocyte during dumping. Histones are essential chromatin components that are preloaded into the oocyte
216 during oogenesis to support the early embryonic cell cycles (Woodland and Adamson, 1977; Günesdogan
217 et al., 2010; Stephenson et al., 2021; Shindo et al., 2022). The oocyte is unusual in that it generates large
218 stores of both replication-dependent and replication-independent histones, which are stable beyond S-phase
219 (Li et al., 2012). Maternal histone loading is of great importance, as histones concentration regulates the
220 progression of early embryonic development (Amodeo et al., 2015; Shindo and Amodeo, 2019; Chari et
221 al., 2019; Shindo and Amodeo, 2021). Like most proteins, replication-dependent histones are synthesized
222 in the nurse cells and transferred to the oocyte during the later stages of oogenesis (Ambrosio and Schedl,
223 1985; Ruddell and Jacobs-Lorena, 1985; Walker and Bownes, 1998). However, a recent study showed that
224 H2Av is transferred to the oocyte as early as stage 9 (Stephenson et al., 2021), suggesting that different
225 histones can behave differently during oogenesis.
226
227 To measure the flow of histones into the oocyte we measured the concentration of H2Av-mRFP in various
228 regions of the egg chamber during nurse cell dumping (Fig. 4D-K). We also segmented the nurse cell nuclei
229 to measure how the nuclear volume and total H2Av-mRFP changed over time (Fig. S3). We found that the
230 nurse cell nuclei lost H2Av-mRFP over time (Fig 4H). However, nuclear volume decreased more rapidly
231 than the H2Av-mRFP loss resulting in a transient increased nuclear concentration (Fig. S3). At the same
232 time, the cytoplasmic intensities of H2Av-mRFP increased in the nurse cells and the anterior and posterior
233 regions of the oocyte with the anterior preceding the posterior (Fig. 4D-E, Movie 12). After completion of
234 dumping, we observed a drop in H2Av-mRFP concentrations both in the anterior and posterior regions of
235 the oocyte (Fig. 4FG, Movie 13), likely due to the dynamic streaming of the oocyte cytoplasm and an
236 increase in the overall volume of the oocyte. Bellymount-PT enabled us to capture the dynamic flux of the
237 maternal proteins in real-time during the later stages of oogenesis
238

239 Along with above key milestones of oogenesis we captured instances of border cell migration (Movie 14),
240 and rotation of egg chamber of in wide range of egg chamber stages (Movie 15,16). Though egg chamber
241 rotation is well documented in stage 5-8 egg chambers (Haigo and Bilder, 2011; Horne-Badovinac, 2014)
242 it appears to continue into stage 9-10 when egg chambers are maintained in vivo (Movie 15, 16). We also
243 observed a novel behavior in egg chambers during stage 12-13 where they appear to slip sidewise rather
244 than a complete rotation (Movie 16). The ability to observe these multiple aspects of egg chamber
245 development highlight the usefulness of Bellymount-PT to explore oogenesis in physiological context.
246
247 **Conclusion**
248 Bellymount-PT provides a powerful means to capture dynamic processes in living animals with minimal
249 perturbation. We have focused on *Drosophila* oogenesis, which is intricately regulated by organismal
250 signals including nutritional availability, mating status, and environmental conditions. While egg chambers
251 can survive in ex vivo culture for a limited time, these systems are unable to faithfully replicate the
252 physiological growth cues, signaling events, and stress response systems found in vivo. The non-invasive
253 nature of Bellymount-PT allows access to internal, sub-cellular details while preserving the native
254 physiological milieu. We can captured all stages of oogenesis and tracked multiple egg chambers for over
255 16 hours, observing progressive developmental stages. The ability to image vitellogenesis, a critical
256 checkpoint in oogenesis that is difficult to study in cultured systems, demonstrates the improved egg
257 chamber health compared to other state of the art techniques.
258
259 One notable constraint of Bellymount-PT is the inability to capture the entire length of oogenesis with
260 normal growth rates. We observed a ~40% mortality rate and decreased fecundity compared to unrestrained
261 flies. A major cause of mortality was drowning in the liquid food within the mounts. Further optimization
262 of the feeding protocol may improve fly health and thereby increase the overall rate of egg chamber
263 development. Another hurdle for fly health during imaging is presented by the common practice of housing
264 microscopes in cool, dark rooms. Increasing the temperature and scheduling imaging sessions to align with
265 the fly circadian rhythm would also likely further increase fecundity. Nonetheless, Bellymount-PT
266 represents a significant improvement in the length of egg chamber growth and survival over existing
267 techniques. Bellymount-PT can be easily implemented in any laboratory equipped with a confocal
268 microscope without requiring specialized equipment. The capability to image multiple females
269 simultaneously increases the throughput and allows multiple genotypes to be imaged under identical
270 conditions. The usefulness of Bellymount-PT is not limited to oogenesis. Indeed, other tissues which are
271 less sensitive to environmental stress cues may be even more amenable to study via Bellymout-PT.

272 Therefore, Bellymount-PT presents an attractive alternative to current ex vivo culture modalities, especially
273 for processes such as yolk uptake that require coordination across multiple tissues.
274
275 **MATERIAL AND METHODS**
276
277 **Fly stocks**
278 *Drosophila* stocks were maintained at room temperature (22±2°C) on standard molasses corn fly media.
279 The following fly stocks were used in this study: w; Mat-α-tub67-gal4, Moesin-GFP/CyO; Mat-α-tub15-
280 gal4, H2Av-mRFP/TM3 (BDSC, 31775) (recombined line received as gift from He Lab, Dartmouth
281 College, NH, USA), w; Mat-α-tub67-gal4/CyO; Mat-α-tub15-gal4, H2Av-mRFP/TM3 (Wieschaus Lab,
282 Princeton University, USA) (Hunter and Wieschaus, 2000), yw; Sp/CyO; EndoH2Av-mCherry/TM3 (a
283 generous gift from Yuki Shindo) (Shindo and Amodeo, under preparation), Yp1-GFP/CyO (VDRC,
284 318746) (Hara and Yamamoto, 2022).
285
286 **Fly mount preparation**
287 The Bellymount imaging system was adapted from Koyama et.al.(2020). 4-5 day old females raised on
288 standard molasses corn fly food supplemented with fresh yeast paste were transferred to apple juice agar
289 plates with fresh yeast paste 12-20 hours before imaging. Healthy and well-fed females were anesthetized
290 on a fly CO_2 pad for mounting. A maximum of five females per experiment were mounted on the glass
291 surface of a 50 mm matTek dish (MatTeck, P50G-1.5-30-F) using clear Elmer's Liquid School Glue
292 (Elmer's, E309). Adherence of the flies to the dish was accomplished as described in Koyama et.al.(2020).
293 A small drop of Elmer's glue was placed on the MatTeck dish near the edge of the glass surface. An
294 anesthetized female was carefully placed on the glue and pressed gently with blunt forceps. The fly was
295 secured by placing a 0.5 cm^2 compression glass starting from her thorax (cut from a 24 x 60 mm cover
296 glass; VWR International, 48393-106). A pair of 2 mm^2 double-sided adhesive spacers of 0.48 mm
297 thickness (Millipore-Sigma , GBL620004-1EA) were placed on either side of the between the compression
298 glass and the dish surface (Fig.1A).
299
300 Flies were provided with a novel liquid food to keep them hydrated and well-fed during long-term imaging.
301 A feeder tube was constructed by bending a 2 cm long glass disposable micropipette (VWR International,
302 53432-921) into a "J" shape using a Bunsen burner. This shape allowed a larger volume of liquid food to
303 be provided to each fly within the space confines of the imaging dish. A wick made from cotton (Equate
304 beauty, 681131169684) was inserted into the short end of the J to allow for the slow release of liquid media.
305 Feeder tubes were filled with freshly made 0.5 mg/ml yeast extract (Thermo Fisher Scientific, BD 212750)

306 in undiluted apple juice (Ocean Spray, 10031200007206). A few grains of active yeast (MP, 02101400-
307 CF) were added to each feeder tube and the tip of the wick was dipped in banana baby food (Gerber,
308 015000076054) immediately before mounting. The feeder tubes were secured with dental wax (Fresh
309 Knight, 40201616938) adjacent to each fly's proboscis so they could feed during imaging intervals. Care
310 was taken to position the feeder tube at an appropriate distance to avoid drowning the fly. A small dollop
311 of yeast paste was provided near the flies' legs to stimulate feeding.
312
313 **Pulsed Anesthesia**
314 For effective anesthetization and to maintain optimum humidity essential for long-term imaging, we
315 covered the sample dish with a 50 mm petri dish lid (Fisher Scientific, 351007). We used this lid instead of
316 the lid of the MatTek dish to increase the depth of the sample dish to allow insertion of moistened absorbent
317 pads (Hazmat Sorbent Pads, S-14748) cut to a diameter of 40 mm with a slit of 15 mm along the diameter
318 and CO_2 tubing. Both were secured with a metal mesh (Genesee Scientific, Flystuff 57-100 Mesh, Stainless
319 Steel 97um) cut to 50 mm diameter. A hole was drilled on the side wall of the lid to allow entry of a 1/16"
320 diameter flexible plastic tube (Millipore Sigma, Z765228) for the administration of CO_2 anesthesia.
321 Through this hole, CO_2 tubing was inserted and glued using KWIK-SIL adhesive silicone glue (World
322 Precision Instruments, 60002) to the wall of the dish. 100% CO_2 at 5 PSI (Airgas®, AS215A320) was
323 bubbled through distilled water in a 500-mL PeCon humidification bottle (PeCon) to increase humidity
324 when CO_2 was administered.
325
326 An Arduino controller (Arduino, 7630049200623) was programmed to open a solenoid valve (Plum
327 Garden, PL-220101) via a rely (TOLAKO, BJ-DT0Y) on receiving a trigger signal for 4 minutes. All time-
328 lapse imaging experiments were conducted on an inverted Zeiss LSM980 microscope controlled by Zen
329 blue (Carl Zeiss, Zen version 3.6). Zen's Experiment Designer module was used to coordinate trigger out
330 signals via an external trigger box (Carl Zeiss, User Interface Box 1437-440) to the Arduino. This module
331 also allowed us to introduce imaging pause and acquisition intervals. At the start of the experiment, we set
332 a trigger out signal to Arduino. Upon receiving the signal from the microscope the Arduino opened the
333 solenoid valve for 4 minutes allowing CO_2 flow into the sample dish. After sending out the trigger-out
334 signal we set a 2 min imaging pause following CO2 inflow. This pause helps the flies succumb to anesthesia
335 before image acquisition. We limited the duration of image acquisition to 2 min when CO_2 to correspond
336 to the anesthesia time. Following completion of imaging the CO_2 was withdrawn. Imaging intervals were
337 set according to the experimental requirement (2 hours for growth rate measurements (Fig.2GH, Fig. 3FH),
338 1 hour for yolk protein uptake (Fig.4A) and 10-11 minutes for H2Av-mRFP (Fig. 4DF)).
339

340 **Microscopy**

341 All the timelapse imaging was conducted on Zeiss LSM980 confocal microscope with Airyscan. The
342 system is equipped with four lasers (405nm, 488nm, 561nm, and 633nm), 2-multi-alkali PMT detectors, a
343 GaAsP detector, and a motorized Axio Observer-7 stage with a z-piezo insert. Images were acquired in
344 Zeiss Multiplex mode (Airyscan MPLX CO-8Y) with either 10x (0.5 NA) air objective or a 20x (0.8 NA)
345 air objective. We were able to reach a Z-depth of ~100 µm with a Z step size ranging from 3-5µm. We
346 utilized the fastest mode of acquisition with pixel time range 0.34 µs - 0.56 µs for 1-2, fluorophore with a
347 pixel sizes ranging from 0.274 x 0.274 x 5 µm - 0.149 x 0.149 x 4 µm respectively. Further details of pixel
348 size, pixel time, fluorophores used, laser setting, imaging intervals are described for each experiment in
349 Table S2.

350

351 Egg chambers used for 3-dimensional reconstructions (Fig. 2CD) were acquired using an upright Olympus
352 FVMPERS multiphoton microscope equipped with the InSight DeepSee Laser System, multi-alkali
353 photomultipliers, two GaAsP detectors, Olympus 25x water immersion objective (XLPLN25×WMP2, NA
354 1.05 531) running FluoView software. We used 920 nm and 1040 nm lasers for GFP and mRFP
355 respectively. We imaged to a Z-depth of 110µm with 3µm step size. Note, this microscope was not
356 equipped for pulsed anesthesia and used to acquire only single time frame images (Fig. 2C-E').

357

358 Brightfield images and recordings of whole flies in the mounts (Fig. 1C,D, Movie. 1-3) were captured using
359 a digital USB-pluggable 60x-250x Digital microscope (Plugable, USB2-MICRO-250X).

360

361 **Fixed egg chamber sample preparation**

362 Ovaries from 5-7 females were dissected in 1% PBS-Tween and fixed in a 1:1 mixture of 4% formaldehyde
363 (Thermo Scientific, 28908) and heptane (Sigma Aldrich, 34873) for 20 min at room temperature. After
364 fixation samples washed 3 times for 10 min each in 0.3% PBS-Tween. Samples were then mounted in a 1:1
365 mixture of Aqua-Poly/Mount (Polysciences, 18606) and RapiClear (SUNJin Lab, RC147001) mounting
366 media. The experiment was performed twice for a total n=15 females. These fixed samples were used to
367 construct a standard growth curve.

368

369 **Image quantification**

370 **Egg chamber midsection area measurements**: Nuclear H2Av-mRFP signal from follicle cells was used
371 to trace the midsection area of the egg chambers using the polygon tool in FIJI (Version 2.14.0/1.54f) (Jia
372 et al., 2016).

373

374 **Staging fixed egg chambers:** Where possible we used size independent criteria to stage egg chambers.
375 Due to lack of suitable markers, egg chambers younger than stage 4 were distinguished based on their size.
376 The chromosome condensation status, which changes from blob-like to dispersed, was used to distinguish
377 stage 4, 5, and 6. Oocyte nuclear position, which moves anteriorly, distinguished stage 6 form 7. Increased
378 proportion of the oocyte area distinguished stages 8-11 along with border cell migration and nurse cell
379 dumping. By the completion of stage 8, the oocyte accounts for 30% of the egg chamber area. The initiation
380 of the border cell migration is an indication of stage 9 and completion of migration identified stage 10. The
381 onset of dumping at stage 11 brings about a dramatic increase in the oocyte size, whereas stages 12 and 13
382 were distinguished based on the appearance of dorsal appendages. Stage 14 is marked by the complete
383 clearance of the nurse cell nuclei (King, 1970). We staged 234 fixed egg chambers and to calculate the
384 frequency distribution of different stages of egg chambers. Further, we also counted the number of egg
385 chambers in each ovariole from these fixed samples (mean number of egg chambers/ovariole (EO) =
386 5.2±0.09 SEM; n=45).
387
388 **Estimating oogenesis timeline to generate growth curve**: We counted the number of ovarioles in a female
389 by dissecting the ovaries from well fed 4-5 days old, mated females in 0.3% PBS-tween. We scored 16
390 females from two independent replicates (mean number of ovarioles per female(O) =35.63±0.46 SEM,
391 n=16), To obtain average number of eggs laid per female per day, we maintained 4-5 days old females and
392 males in individual pairs in fresh food vials supplemented with fresh yeast paste and recorded the number
393 of eggs of laid by individual females in 24 hours. We recorded the fecundity of 8 females from two
394 replicates (mean number of eggs laid per female/day (E)=51.5±2.65 SEM; n=8). This gave us an egg
395 production rate per ovariole (EPR = E/O) (David and Merle, 1968; King, 1970; Spradling, 1993) off 1.45
396 eggs per day by an individual ovariole (EPR = E/O) From this we estimated the total time required for
397 progression from stage 2 to stage (G = EO/EPR) as 86 hours. Finally, we calculated the growth duration of
398 an egg chamber at a specific stage (Gs) based on the frequency with which it occurred in our samples (eg.
399 since 7.7% of our egg chambers were in stage 8, Gs_8 = 6.65 h). The frequency of distribution for all stages
400 and their corresponding development time is given in Table S1.
401
402 With the estimated duration for the individual stage and the midsection area we fit a standard exponential
403 growth curve: $A = 273\ e^{0.06t}$, where t=time in hours, A=area in μm^2. From this equation, we calculate the
404 expected time t_0 (initial age of the egg chamber at the being of the imaging session) for the known area
405 measurements for each time lapse image in Fig. 2G-H and Fig.3F-H.
406

407 The increase in egg chamber growth declines past stage 10, we considered the percent of the egg chamber
408 area occupied by the oocyte to fine tune the staging of the egg chambers for yolk uptake and histone transfer
409 experiments (Fig. 4). Therefore, we generated a standard exponential growth curve based on oocyte percent
410 for the stages 8-11 using measured oocyte percent and the estimated duration from fixed samples (n=44).
411 Here is the exponential equation for the oocyte percent: $O = 0.318\ e^{0.07t}$, where t=time in hours, O=oocyte
412 percent. From this equation we calculated the expected time t_0 (initial age of the egg chamber at the start of
413 the imaging session) from the know oocyte percent of the live imaged samples of Yp1 and H2Av
414 quantification experiments. .We also calculated the correlation for oocyte percent and egg chamber area
415 (Fig. S3A) to make sure egg chamber midsection area and oocyte percent are positively correlated..
416
417 **Yolk proteins quantification.** To quantify the sfGFP-tagged yolk protein, we drew the region of interest
418 (ROI) around the oocyte using the H2Av-mCherry signal. Due to our inability to image the full depth of
419 the older egg chambers, we considered one-half of the egg chambers for quantification (top through
420 midsection). We measured the total intensity of GFP for all the z slices across one-half of the egg chamber.
421 Similarly, we measured the total intensities of H2Av-mCherry from the follicle cells to normalize the GFP
422 intensities and obtain normalized total Yp1 intensities over the developmental duration.
423
424 **H2Av-mRFP quantifications**. To quantify the total nuclear H2Av-mRFP intensities and volume of the
425 nurse cell nuclei (Fig. 4G-K) we segmented 1-2 posterior nuclei per egg chamber in 3 dimensions using a
426 custom-built FIJI macro which apply Gaussian Blur in 3D (5,5,1) and set an automatic threshold based on
427 Otsu method to generate masks. These masks were further processed by applying erode, dilate, open, close,
428 fill holes functions to refine the segmentation of the nuclear signal across the Z-stacks. Processed masks
429 were converted to ROIs using analyze particles function. These ROIs were used to measure the nuclear area
430 and pixel intensities.
431
432 To estimate how local concentrations change over time (Fig. 4E,G,I-K, S3B) we measured average pixel
433 intensity in 20x20 pixel (428.5 µm) regions in a set of 3 Z-slices (step size 3 µm) starting 9µm below the
434 follicle cell border. Nurse cell cytoplasm was defined as a nuclear free region next to the quantified nucleus
435 within a distance of 100 pixel (17µm) from the oocyte border. "Anterior oocyte cytoplasm" was defined
436 as a nuclear-free region within 100 pixels (17µm) from the border of nurse cells on the oocyte side.
437 "Posterior oocyte cytoplasm" was defined as a region within 100 pixels (17µm) from the posterior border
438 of egg. We manually placed the ROI at each timepoint to ensure ROI was placed in a relative consistent
439 region across the image duration since the sample moved in all three planes during the imaging intervals.

The nurse cell nuclear and cytoplasmic and oocyte cytoplasmic intensities were normalized to follicle cell intensities.

3D surface reconstruction. H2Av-mRFP signal from of the nurse cell nuclei was used to reconstruct the nuclear surfaces, while follicle cell nuclei were used to reconstruct surfaces for the whole egg chambers using the Arivis Vision4D program (version 4.0) (Fig. 2C). An analysis pipeline consisting of blob finder was used to segment nuclear signal based on size thresholding. Further, split threshold was set to avoid merging the of signals or over-segmentation. H2Av-mRFP signal on the surface of the egg chambers was used to train the Arivis machine learning based draw tool. Segmentation errors were corrected manually.

Figure preparation. Images were processed in FIJI for figure preparation (Figures 1F,G, 2C,D,F-H, 3F,H, 4A,D,F, S4) using the following functions: Subtract background with a radius of 50-100 pixels, Gaussian blur of radius 0.5-1 pixels, and a Median blur of radius 1-2 (Jackson et al., 2023b). Note, all quantifications were performed on unaltered images. Fig. S4 compares the unprocessed and processed images. Exponential growth curves and graphical presentation of data were prepared out in Python environment. Pictorial presentations and figure panel were prepared in Adobe Illustrator (Version 27.9).

Statistics

P-values for fecundity and different liquid food diet (Fig. 2B, S1) were derived from a student t-test using Microsoft Excel (Version 16.83). The number of biological replicates are indicated in the figure legends and text.

ACKNOWLEDGMENTS

We thank Lucy O'Brien and Leslie Koyama for sharing the original Bellymount technology. We thank members of the O'Brien lab, Rocky Diegmiller, members of the Amodeo lab and participants of the GSA DGRC-2023 meeting for constructive comments. We also thank Pat Robison, Ann Lavanway, Bing He, The Dartmouth bio-MT Molecular Interactions & Imaging Core and the Life Sciences Light Microscopy Facility for help with image acquisition and analysis and Robert Robertson for help with the Arduino anesthesia system. We appreciate Yuki Shindo for sharing a Drosophila stock (w; Sp/CyO; EndogenousH2Av-mCherry). This work was supported by NIH NIGMS MIRA (1R35GM150853-01) and NIH NIGMS COBRE award (P20-GM113132).

Competing interests

The authors declare no competing or financial interests.

Author Contributions

Conceptualization: S.B., A.A.; Methodology: S.B.; Validation: S.B., A.A.; Formal analysis: S.B.; Investigation: S.B., AA.; Resources: AA.; Data curation: S.B.; Writing-original draft: S.B., A.A.; Writing-review editing: S.B., A.A.; Supervision: A.A.; Project administration: A.A.; Funding acquisition: A.A.

.

Funding

This work was supported by NIH NIGMS MIRA (1R35GM150853-01) and NIH NIGMS COBRE award (P20-GM113132).

Data availability

All relevant data can be found within the article and its supplementary information. The codes for CO_2 pulsing and imaging analysis will be provided on request.

REFERENCES

Ambrosio, L. and Schedl, P. (1985). Two discrete modes of histone gene expression during oogenesis in Drosophila melanogaster. *Dev Biol* **111**, 220–231.

Amodeo, A. A., Jukam, D., Straight, A. F. and Skotheim, J. M. (2015). Histone titration against the genome sets the DNA-to-cytoplasm threshold for the Xenopus midblastula transition. *Proceedings of the National Academy of Sciences* **112**, E1086–E1095.

Avilés-Pagán, E. E., Kang, A. S. W. and Orr-Weaver, T. L. (2020). Identification of New Regulators of the Oocyte-to-Embryo Transition in Drosophila. *G3 (Bethesda)* **10**, 2989–2998.

Brubaker-Purkey, B. J. and Woodruff, R. I. (2013). Vitellogenesis in the Fruit Fly, Drosophila melanogaster: Antagonists Demonstrate that the PLC, IP3/DAG, PK-C Pathway is Triggered by Calmodulin. *J Insect Sci* **13**, 68.

Chari, S., Wilky, H., Govindan, J. and Amodeo, A. A. (2019). Histone concentration regulates the cell cycle and transcription in early development. *Development* **146**, dev177402.

503 **Dapples, C. C. and King, R. C.** (1970). The development of the nucleolus of the ovarian nurse
504 cell of Drosophila melanogaster. *Z Zellforsch Mikrosk Anat* **103**, 34–47.

505 **David, L. and Merle, J.** (1968). A reevaluation of the duration of egg chamber stages in
506 oogenesis of Drosophila melanogaster.

507 **Diegmiller, R., Doherty, C. A., Stern, T., Imran Alsous, J. and Shvartsman, S. Y.** (2021).
508 Size scaling in collective cell growth. *Development* **148**, dev199663.

509 **Fuhrmann, M., Gockel, N., Arizono, M., Dembitskaya, Y., Nägerl, U. V., Pennacchietti, F.,**
510 **Damenti, M., Testa, I. and Willig, K. I.** (2022). Super-Resolution Microscopy Opens
511 New Doors to Life at the Nanoscale. *J. Neurosci.* **42**, 8488–8497.

512 **Günesdogan, U., Jäckle, H. and Herzig, A.** (2010). A genetic system to assess in vivo the
513 functions of histones and histone modifications in higher eukaryotes. *EMBO Rep* **11**,
514 772–776.

515 **Gutzeit, H. and Koppa, R.** (1982). Time-lapse film analysis of cytoplasmic streaming during
516 late oogenesis of Drosophila. *Development*.

517 **Haigo, S. L. and Bilder, D.** (2011). Global tissue revolutions in a morphogenetic movement
518 controlling elongation. *Science* **331**, 1071–1074.

519 **Hara, Y. and Yamamoto, D.** (2022). Effects of Food and Temperature on Drosophila
520 melanogaster Reproductive Dormancy as Revealed by Quantification of a GFP-Tagged
521 Yolk Protein in the Ovary. *Frontiers in Physiology* **12**,.

522 **He, L., Wang, X. and Montell, D. J.** (2011). Shining light on Drosophila oogenesis: live
523 imaging of egg development. *Curr Opin Genet Dev* **21**, 612–619.

524 **Horne-Badovinac, S.** (2014). The Drosophila Egg Chamber—A New Spin on How Tissues
525 Elongate. *Integr Comp Biol* **54**, 667–676.

526 **Hunter, C. and Wieschaus, E.** (2000). Regulated expression of nullo is required for the
527 formation of distinct apical and basal adherens junctions in the Drosophila blastoderm. *J*
528 *Cell Biol* **150**, 391–401.

529 **Imran Alsous, J., Romeo, N., Jackson, J. A., Mason, F. M., Dunkel, J. and Martin, A. C.**
530 (2021). Dynamics of hydraulic and contractile wave-mediated fluid transport during
531 Drosophila oogenesis. *Proceedings of the National Academy of Sciences* **118**,
532 e2019749118.

533 **Inaki, M., Vishnu, S. and Matsuno, K.** (2022). Live imaging of delamination in Drosophila
534 shows epithelial cell motility and invasiveness are independently regulated. *Sci Rep* **12**,
535 16210.

536 **Isasti-Sanchez, J., Münz-Zeise, F., Lancino, M. and Luschnig, S.** (2021). Transient opening
537 of tricellular vertices controls paracellular transport through the follicle epithelium during
538 *Drosophila* oogenesis. *Developmental Cell* **56**, 1083-1099.e5.

539 **Jackson, J. A., Denk-Lobnig, M., Kitzinger, K. A. and Martin, A. C.** (2023a). Change in
540 RhoGAP and RhoGEF availability drives transitions in cortical patterning and
541 excitability in Drosophila. *bioRxiv* 2023.11.06.565883.

542 **Jackson, J. A., Romeo, N., Mietke, A., Burns, K. J., Totz, J. F., Martin, A. C., Dunkel, J.**
543 **and Imran Alsous, J.** (2023b). Scaling behaviour and control of nuclear wrinkling. *Nat.*
544 *Phys.* **19**, 1927–1935.

545 **Jia, D., Xu, Q., Xie, Q., Mio, W. and Deng, W.-M.** (2016). Automatic stage identification of
546 Drosophila egg chamber based on DAPI images. *Sci Rep* **6**, 18850.

547 **King, R. C.** (1970). *OVARIAN DEVELOPMENT*. New York, NY: Academic Press.

548 **Koyama, L. A. J., Aranda-Díaz, A., Su, Y.-H., Balachandra, S., Martin, J. L., Ludington,**
549 **W. B., Huang, K. C. and O'Brien, L. E.** (2020). Bellymount enables longitudinal,
550 intravital imaging of abdominal organs and the gut microbiota in adult Drosophila. *PLOS*
551 *Biology* **18**, e3000567.

552 **Lebo, D. P. V. and McCall, K.** (2021). Murder on the Ovarian Express: A Tale of Non-
553 Autonomous Cell Death in the Drosophila Ovary. *Cells* **10**, 1454.

554 **Lei, F., Xu, X., Huang, J., Su, D. and Wan, P.** (2023). Drosophila RhoGAP18B regulates actin
555 cytoskeleton during border cell migration. *PLOS ONE* **18**, e0280652.

556 **Li, Z., Thiel, K., Thul, P. J., Beller, M., Kühnlein, R. P. and Welte, M. A.** (2012). Lipid
557 Droplets Control the Maternal Histone Supply of *Drosophila* Embryos. *Current Biology*
558 **22**, 2104–2113.

559 **Lu, W. and Gelfand, V. I.** (2022). Go with the flow – bulk transport by molecular motors. *J*
560 *Cell Sci* **136**, jcs260300.

561 **Marchetti, M., Zhang, C. and Edgar, B. A.** (2022). An improved organ explant culture method
562 reveals stem cell lineage dynamics in the adult Drosophila intestine. *eLife* **11**, e76010.

563 **Martin, J. L., Sanders, E. N., Moreno-Roman, P., Jaramillo Koyama, L. A., Balachandra,**
564 **S., Du, X. and O'Brien, L. E.** (2018). Long-term live imaging of the Drosophila adult
565 midgut reveals real-time dynamics of division, differentiation and loss. *eLife* **7**, e36248.

566 **Miao, G., Guo, L. and Montell, D. J.** (2022). Border cell polarity and collective migration
567 require the spliceosome component Cactin. *J Cell Biol* **221**, e202202146.

568 **Morris, J. and Lehmann, R.** (1999). Drosophila oogenesis: Versatile spn doctors. *Current*
569 *Biology* **9**, R55–R58.

570 **Morris, L. X. and Spradling, A. C.** (2011). Long-term live imaging provides new insight into
571 stem cell regulation and germline-soma coordination in the Drosophila ovary.
572 *Development* **138**, 2207–2215.

573 **Parsons, T. T., Mosallaei, S. and Raftery, L. A.** (2023). Two phases for centripetal migration
574 of Drosophila melanogaster follicle cells: initial ingression followed by epithelial
575 migration. *Development* **150**, dev200492.

576 **Peters, N. C. and Berg, C. A.** (2016). In vitro culturing and live imaging of Drosophila egg
577 chambers: A history and adaptable method. *Methods Mol Biol* **1457**, 35–68.

578 **Petri, W. H., Mindrinos, M. N., Lombard, M. F. and Margaritis, L. H.** (1979). In vitro
579 development of theDrosophila chorion in a chemically defined organ culture medium.
580 *Wilhelm Roux' Archiv* **186**, 351–362.

581 **Poinapen, D., Konopka, J. K., Umoh, J. U., Norley, C. J. D., McNeil, J. N. and Holdsworth,**
582 **D. W.** (2017). Micro-CT imaging of live insects using carbon dioxide gas-induced
583 hypoxia as anesthetic with minimal impact on certain subsequent life history traits. *BMC*
584 *Zoology* **2**, 9.

585 **Prasad, M. and Montell, D. J.** (2007). Cellular and Molecular Mechanisms of Border Cell
586 Migration Analyzed Using Time-Lapse Live-Cell Imaging. *Developmental Cell* **12**, 997–
587 1005.

588 **Richard, D. S., Watkins, N. L., Serafin, R. B. and Gilbert, L. I.** (1998). Ecdysteroids regulate
589 yolk protein uptake by *Drosophila melanogaster* oocytes. *Journal of Insect Physiology*
590 **44**, 637–644.

591 **Row, S., Huang, Y.-C. and Deng, W.-M.** (2021). Developmental regulation of oocyte lipid
592 intake through 'patent' follicular epithelium in Drosophila melanogaster. *iScience* **24**,
593 102275.

594 **Ruddell, A. and Jacobs-Lorena, M.** (1985). Biphasic pattern of histone gene expression during
595 Drosophila oogenesis. *Proc Natl Acad Sci U S A* **82**, 3316–3319.

596 **Shen, J., Yang, P., Zhu, X., Gu, Y., Huang, J. and Li, M.** (2020). CO2 anesthesia on
597 Drosophila survival in aging research. *Archives of Insect Biochemistry and Physiology*
598 **103**, e21639.

599 **Shimada, Y., Burn, K. M., Niwa, R. and Cooley, L.** (2011). Reversible response of protein
600 localization and microtubule organization to nutrient stress during Drosophila early
601 oogenesis. *Developmental Biology* **355**, 250–262.

602 **Shindo, Y. and Amodeo, A. A.** (2019). Dynamics of Free and Chromatin-Bound Histone H3
603 during Early Embryogenesis. *Curr Biol* **29**, 359-366.e4.

604 **Shindo, Y. and Amodeo, A. A.** (2021). Excess histone H3 is a competitive Chk1 inhibitor that
605 controls cell-cycle remodeling in the early Drosophila embryo. *Curr Biol* **31**, 2633-
606 2642.e6.

607 **Shindo, Y., Brown, M. G. and Amodeo, A. A.** (2022). Versatile roles for histones in early
608 development. *Curr Opin Cell Biol* **75**, 102069.

609 **Soller, M., Haussmann, I. U., Hollmann, M., Choffat, Y., White, K., Kubli, E. and Schäfer,**
610 **M. A.** (2006). Sex-peptide-regulated female sexual behavior requires a subset of
611 ascending ventral nerve cord neurons. *Curr Biol* **16**, 1771–1782.

612 **Spradling, A. C.** (1993). *The development of Drosophila melanogaster*. New York: Cold Spring
613 Habor Laboratory Press.

614 **Stephenson, R. A., Thomalla, J. M., Chen, L., Kolkhof, P., White, R. P., Beller, M. and**
615 **Welte, M. A.** (2021). Sequestration to lipid droplets promotes histone availability by
616 preventing turnover of excess histones. *Development* **148**, dev199381.

617 **Tang, R., Qin, P., Liu, X., Wu, S., Yao, R., Cai, G., Gao, J., Wu, Y. and Guo, Z.** (2021).
618 Intravital imaging strategy FlyVAB reveals the dependence of Drosophila enteroblast
619 differentiation on the local physiology. *Commun Biol* **4**, 1–12.

620 **Terashima, J. and Bownes, M.** (2004). Translating available food into the number of eggs laid
621 by Drosophila melanogaster. *Genetics* **167**, 1711–1719.

622 **Tsao, C.-K., Ku, H.-Y., Lee, Y.-M., Huang, Y.-F. and Sun, Y. H.** (2016). Long Term Ex Vivo
623 Culture and Live Imaging of Drosophila Larval Imaginal Discs. *PLOS ONE* **11**,
624 e0163744.

625 **Walker, J. and Bownes, M.** (1998). The expression of histone genes during Drosophila
626 melanogaster oogenesis. *Dev Genes Evol* **207**, 535–541.

627 **Weichselberger, V., Dondl, P. and Classen, A.-K.** (2022). Eya-controlled affinity between cell
628 lineages drives tissue self-organization during Drosophila oogenesis. *Nat Commun* **13**,
629 6377.

630 **Wilcockson, S. G. and Ashe, H. L.** (2021). Live imaging of the *Drosophila* ovarian germline
631 stem cell niche. *STAR Protocols* **2**, 100371.

632 **Williams, A. M., Donoughe, S., Munro, E. and Horne-Badovinac, S.** (2022). Fat2 polarizes
633 the WAVE complex in trans to align cell protrusions for collective migration. *eLife* **11**,
634 e78343.

635 **Woodland, H. R. and Adamson, E. D.** (1977). The synthesis and storage of histones during the
636 oogenesis of Xenopus laevis. *Dev Biol* **57**, 118–135.

637 **Yalonetskaya, A., Mondragon, A. A., Hintze, Z. J., Holmes, S. and McCall, K.** (2020).
638 Nuclear degradation dynamics in a nonapoptotic programmed cell death. *Cell Death*
639 *Differ* **27**, 711–724.

640 **Zajac, A. L., Williams, A. M. and Horne-Badovinac, S.** (2023). A Low-Tech Flow Chamber
641 for Live Imaging of Drosophila Egg Chambers During Drug Treatments. *Methods Mol*
642 *Biol* **2626**, 277–289.

643 **Zhang, S.-Q. and Liu, J.-L.** (2024). Dynamic Cytoophidia during Late-Stage Drosophila
644 Oogenesis. *International Journal of Molecular Sciences* **25**, 2575.

645
646
647
648
649
650
651
652
653
654

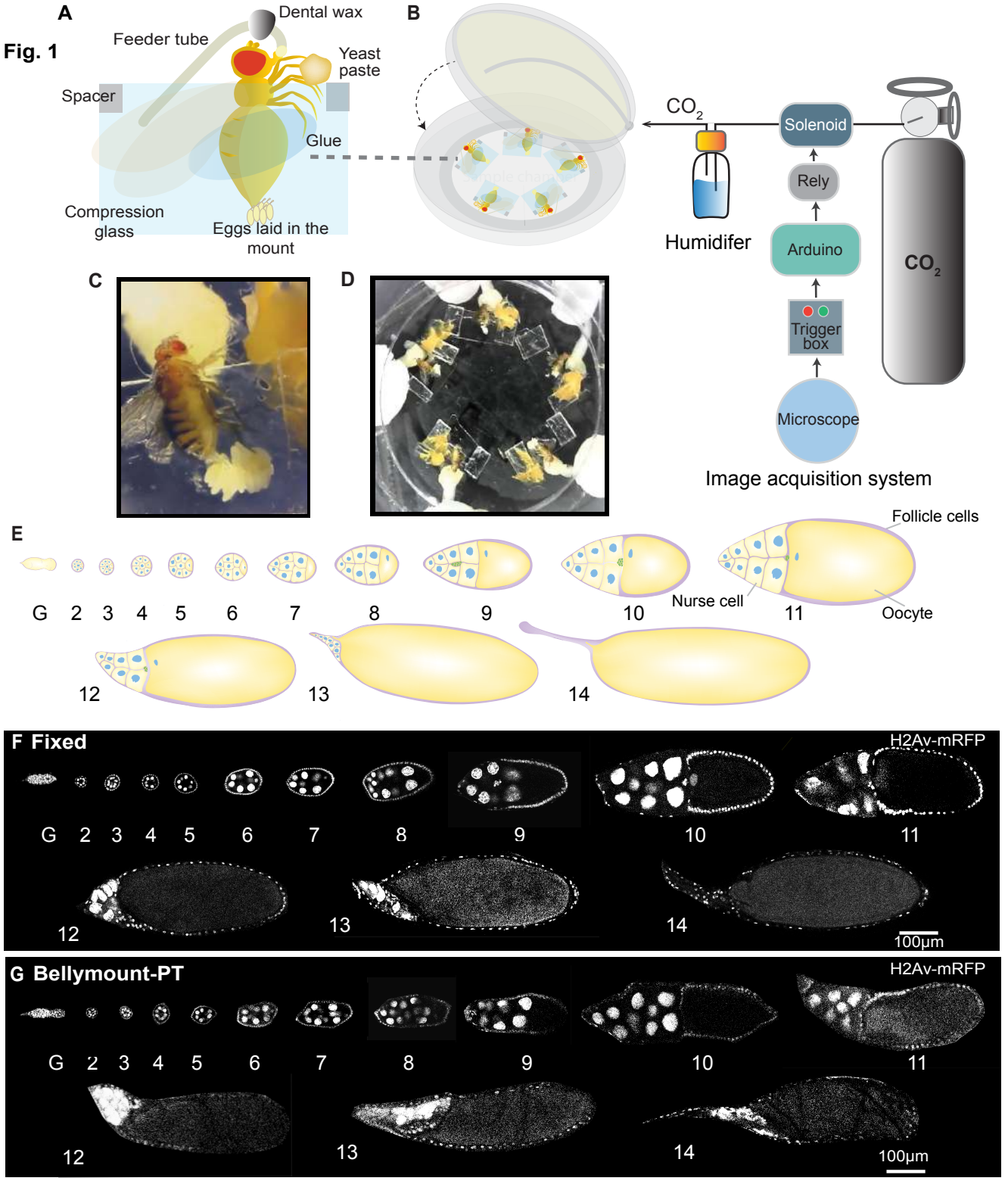
Fig. 1
A
Dental wax
Feeder tube
Yeast paste
Spacer
Glue
Compression glass
Eggs laid in the mount
B
CO2
Solenoid
Rely
Arduino
Trigger box
Microscope
Humidifer
CO2
Image acquisition system
C
D
E
Follicle cells
Nurse cell
Oocyte
G 2 3 4 5 6 7 8 9 10 11 12 13 14
F Fixed
H2Av-mRFP
100μm
G Bellymount-PT
H2Av-mRFP
100μm

655

656 **FIGURE LEGENDS**

657

658 **Fig. 1. Bellymount-Pulsed Tracking (PT) allows long-term live imaging of oogenesis in live females.**
659 (A) Schematic of a fly mounted for Bellymount-Pulsed Tracking (Bellymount-PT). Mated and well-fed
660 females were glued on the cover-glass surface of a MatTek dish using Elmer's glue and compressed
661 between the dish and the glass coverslip with 0.48 mm spacers to secure the fly during imaging. A small
662 amount of fresh yeast paste and a feeder tube containing custom liquid apple juice, yeast extract food ensure
663 proper nutrition. (B) Image acquisition setup for confocal microscope and pulsed CO_2 anesthetize. An
664 Arduino programmed to regulate the CO_2 flow via solenoid value is connected to a signal from the
665 microscope. CO_2 is pulsed into the sample dish for four minutes during acquisition through a humidifying
666 chamber. Flies are allowed to awaken and feed between time points. (C) A live female that remained alive
667 and fecund after 16 hours in the mount without imaging. Note the large number of eggs which have
668 accumulated to the posterior of the fly. (D) Whole mount with flies and feeder tubes. Five females can be
669 imaged in the same dish simultaneously. (E) Schematic showing oogenesis stages. The blue circles
670 represent the nurse cells and the oocyte nuclei, the pink border represents the follicle cell layer, and the
671 cells in green represent border cells. (F) Staged fixed egg chambers expressing H2Av-mRFP from multiple
672 females were imaged at 20x (0.8 NA) on Zeiss LSM980. (G) Collection of staged live egg chambers
673 expressing H2Av-mRFP from multiple females acquired using Bellymount-PT imaged on the same
674 microscope as F. These egg chambers were imaged through the intact cuticle of the female abdomen.
675 Adjacent egg chambers were cropped out and images were processed for presentation using background
676 subtraction, gaussian filter and median filters in Fiji.

677

678

679

680

681

682

683

684

685

686

687

688

Fig. 2

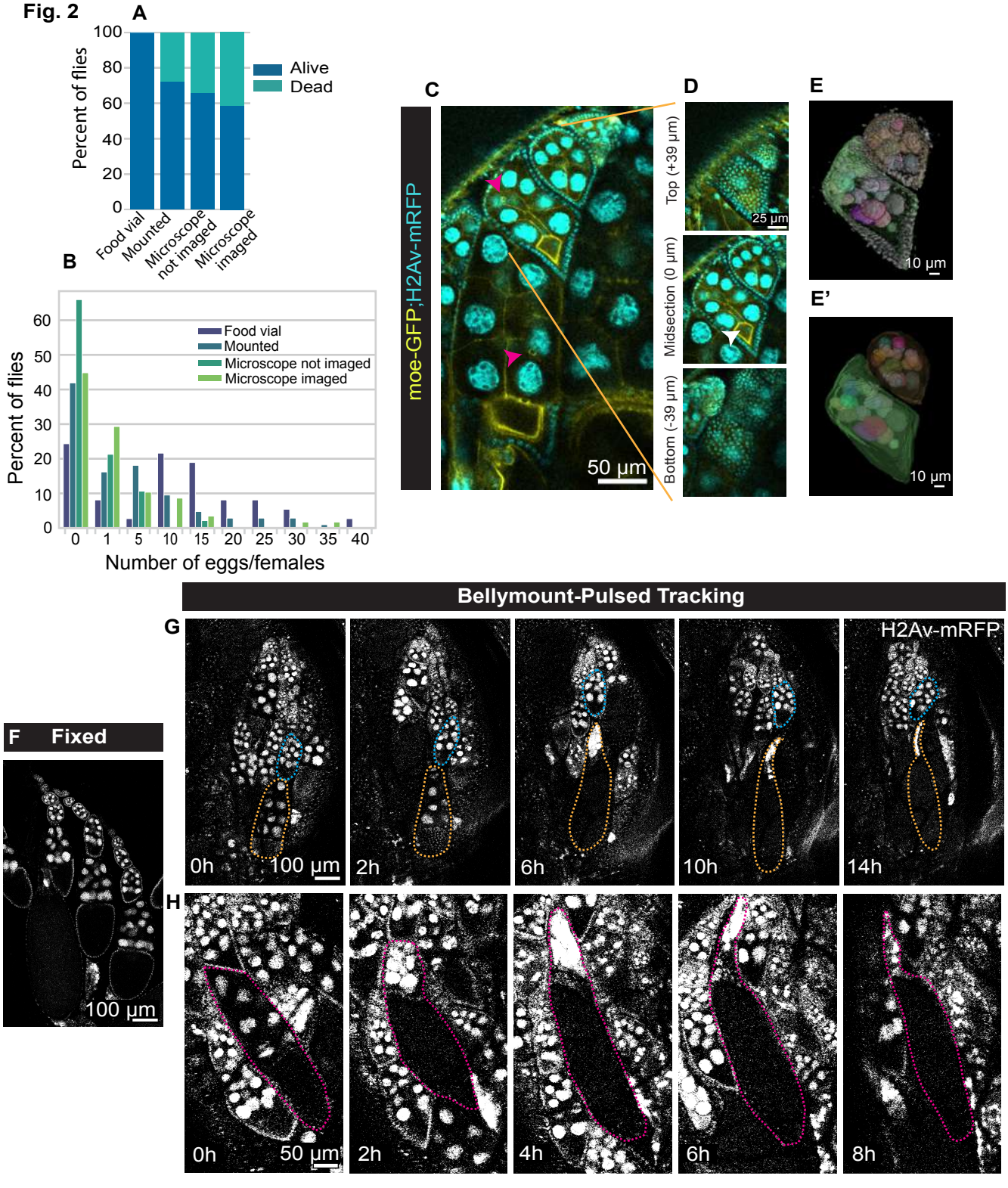
A
Percent of flies
100
80
60
40
20
0
Alive
Dead
Food vial
Mounted
Microscope not imaged
Microscope imaged
B
Percent of flies
60
50
40
30
20
10
0
Food vial
Mounted
Microscope not imaged
Microscope imaged
0
1
5
10
15
20
25
30
35
40
Number of eggs/females
C
moe-GFP;H2Av-mRFP
50 µm
D
Top (+39 µm)
25 µm
Midsection (0 µm)
Bottom (-39 µm)
E
10 µm
E'
10 µm
Bellymount-Pulsed Tracking
G
H2Av-mRFP
0h
100 µm
2h
6h
10h
14h
F
Fixed
100 µm
H
0h
50 µm
2h
4h
6h
8h

Fig. 2. Pulsed anesthesia allows tracking for over 14 hours. (A) Survival percentage for females after 16 hours of imaging compared to various controls. To understand the effect of mounting, anesthesia, and laser exposure we compared imaged flies (n=58) to controls that were either never placed in the Bellymount-PT chamber (food vial, n=37); mounted, but never exposed to the imaging protocol (mounted, n=105), and those that were placed on the microscope during imaging, anesthetized but not exposed to laser (microscope, not imaged n=47). Most of the observed mortality can be attributed to the restraints, though anesthesia and exposure to laser further decrease survival. (B) Histogram of eggs laid in 16-hour period for the same flies as in A. Females laid 0-40 eggs during the imaging period. Flies that remained in their food vials laid an average of 10 eggs per female while flies imaged laid 2 eggs on average. (C) Single time point (not time-lapse) representative image of multiple egg chambers within a single ovariole expressing H2Av-mRFP and Moesin-GFP using Bellymount-PT acquired on Olympus multiphoton microscope (25x water objective). (D) All three cell types (oocyte, nurse, and follicle cells) can be visualized through the cuticle. There is sufficient z-resolution to ~ 80 µm to capture the full volume of egg chambers stage 8 and younger. Pink arrowheads indicate ring canals and white indicates oocyte nucleus. Insets represent the top (+39µm), midsection (0µm), and bottom (-39µm) z-slices of a stage 6 egg chamber. (E,E') 3D reconstruction of the egg chambers in C with nuclear H2Av-mRFP signal and the 3D constructed surface. (F) Fixed egg chambers with the same genotype and imaging as G-H for comparison. (G-H) Live, developing egg chambers expressing H2Av-mRFP imaged over time using Bellymount-PT. (G) Multiple egg chambers can be tracked in a single experiment. The egg chamber marked in blue starts in early stage 8 and increased in size over the imaging duration. The egg chamber marked in yellow starts in stage 10 and progresses through stage 14 with complete dorsal appendages formation visible by 14 hours. (H) Egg chamber marked in magenta shows the progression the of egg chamber from stages 10-14. Images in F-D were imaged on Zeiss LSM980 microscope with a 10x air objective. Images in the (C-H) were processed for presentation using background subtraction, gaussian filter and median filters in Fiji.

Fig 3

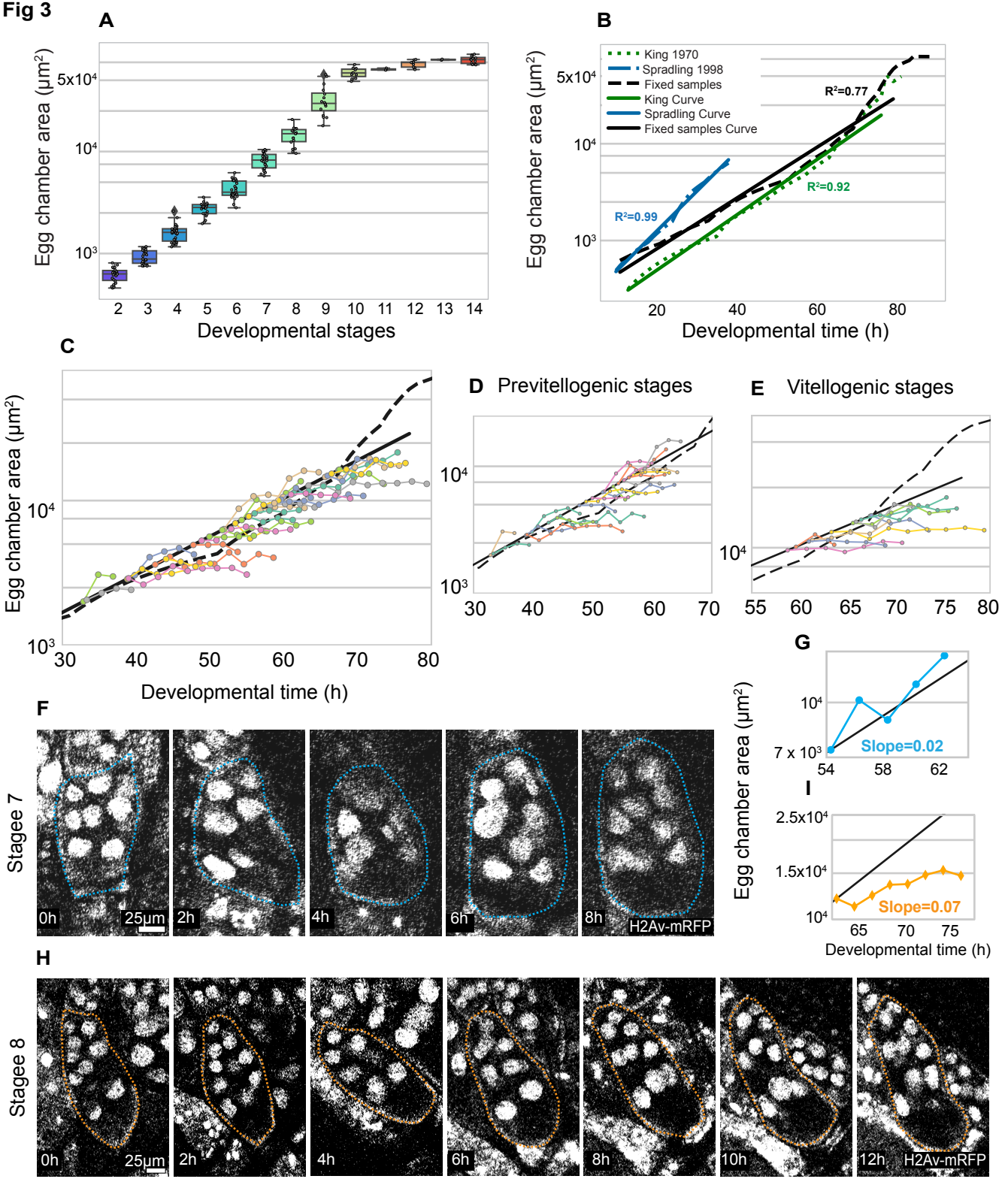
A
Egg chamber area (µm²)
5x10⁴
10⁴
10³
2 3 4 5 6 7 8 9 10 11 12 13 14
Developmental stages
B
King 1970
Spradling 1998
Fixed samples
King Curve
Spradling Curve
Fixed samples Curve
R²=0.77
R²=0.92
R²=0.99
Egg chamber area (µm²)
5x10⁴
10⁴
10³
20 40 60 80
Developmental time (h)
C
Egg chamber area (µm²)
10⁴
10³
30 40 50 60 70 80
Developmental time (h)
D Previtellogenic stages
10⁴
10³
30 40 50 60 70
E Vitellogenic stages
10⁴
55 60 65 70 75 80
F
Stagee 7
0h
25µm
2h
4h
6h
8h
H2Av-mRFP
G
Egg chamber area (µm²)
10⁴
7 x 10³
Slope=0.02
54 58 62
I
2.5x10⁴
1.5x10⁴
10⁴
Slope=0.07
65 70 75
Developmental time (h)
H
Stagee 8
0h
25µm
2h
4h
6h
8h
10h
12h
H2Av-mRFP

723 **Fig. 3. Bellymount-PT allows live monitoring of egg chamber growth. (A)** The midsection area of fixed
724 egg chambers by stage. Fixed egg chambers were staged based on milestones of oogenesis as per (King
725 1970; see methods). The measured sizes combined with the frequency of each stage, total number of egg
726 chambers per ovariole, and the number of eggs laid by individual females in 24 hours were used to construct
727 a standard growth curve (black line panel B) for the fly line we used for live growth analysis (w; Mat-α-
728 tub67-gal4/CyO; Mat-α-tub15-gal4, H2Av-mRFP/TM3) (B) Comparison of standard growth curves from
729 this study and previous literature derived from fixed samples. Egg chamber areas from King et al 1970
730 (green) and Spradling 1993 (blue) were used to generate an exponential standard growth curve along with
731 the corresponding time estimates. (C) The midsection area of 38 egg chambers tracked using Bellymount-
732 PT with 2 hour imaging intervals. The resulting traces were aligned to the standard growth curve shown in
733 B (black) by their initial (t0) area and with subsequent timepoints based on actual image acquisition times.
734 Individual egg chambers were tracked for 4-18 hours. (D) A subset of the area traces in C that begin in the
735 previtellogenic stages (4-7). (E) A subset of the area traces in C that begin at the start of the vitellogenic
736 stages (stage 8). (F) A previtellogenic egg chamber starting at stage 7. (G) The change in midsection area
737 over time for the egg chamber in E compared to the standard growth curve in black. Note the agreement
738 between predicted and observed growth rates. (H) A vitellogenic stage 8 egg chamber tracked for about 12
739 hours. (I) The growth rate of the egg chamber in H compared to the standard curve. Note that growth is
740 slower than predicted. (F and H) were processed for presentation using background subtraction, gaussian
741 filter and median filters in Fiji.
742
743
744
745
746
747
748
749
750
751
752
753
754
755

Fig 4

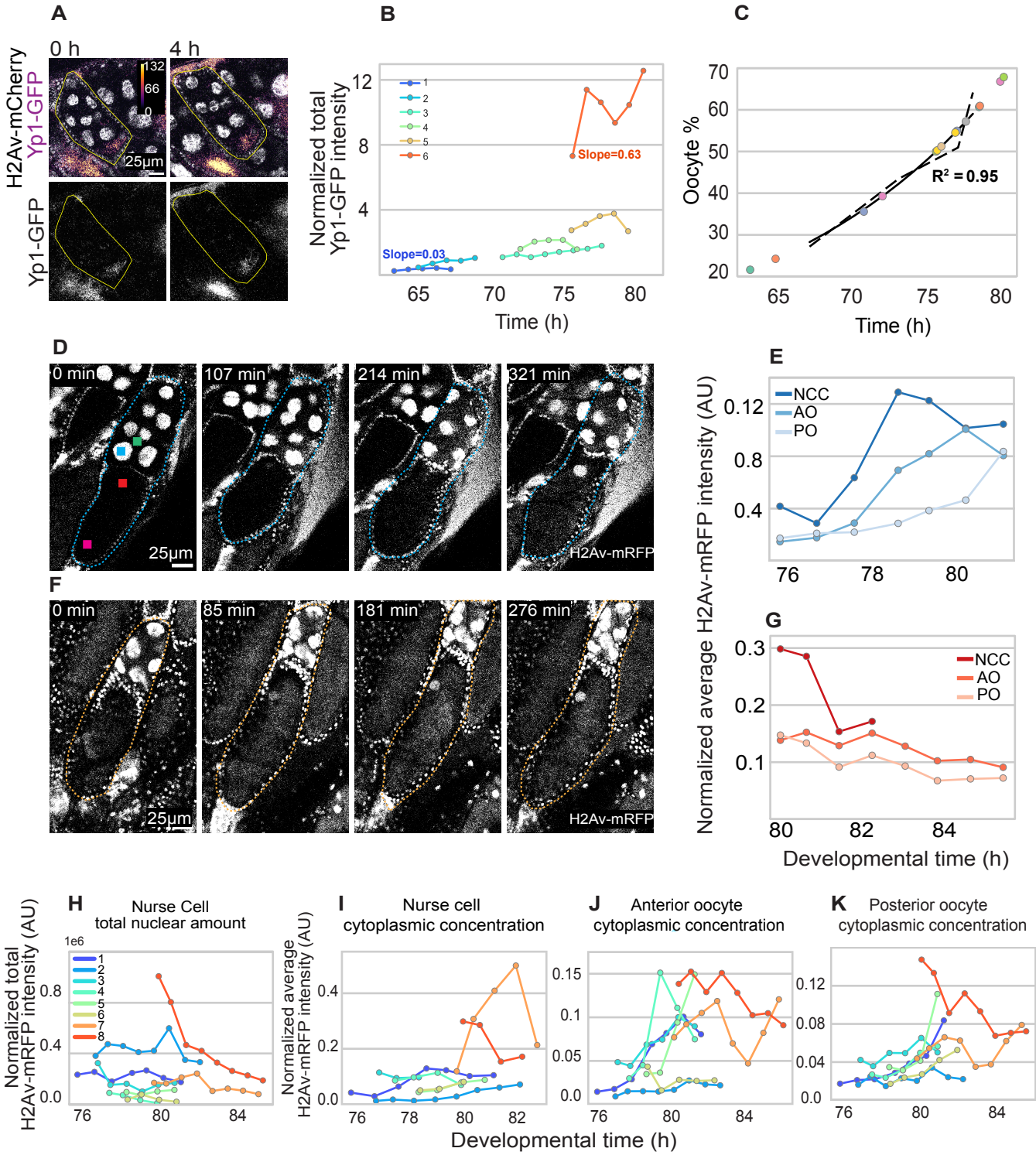
A
0 h
4 h
H2Av-mCherry
Yp1-GFP
132
66
0
25µm
Yp1-GFP
B
Normalized total Yp1-GFP intensity
Slope=0.63
Slope=0.03
Time (h)
C
Oocyte %
R² = 0.95
Time (h)
D
0 min
107 min
214 min
321 min
25µm
H2Av-mRFP
E
NCC
AO
PO
F
0 min
85 min
181 min
276 min
25µm
H2Av-mRFP
G
NCC
AO
PO
Normalized average H2Av-mRFP intensity (AU)
Developmental time (h)
H
Nurse Cell total nuclear amount
Normalized total H2Av-mRFP intensity (AU)
1e6
I
Nurse cell cytoplasmic concentration
Normalized average H2Av-mRFP intensity (AU)
J
Anterior oocyte cytoplasmic concentration
K
Posterior oocyte cytoplasmic concentration
Developmental time (h)

Fig. 4. Bellymount-PT allows for the observation of dynamic events during oogenesis. (A) Yolk protein accumulation during vitellogenic stages was tracked in flies expressing Yp1:GFP. (B) Quantification of the total Yp1:GFP intensity in the oocyte over time for 6 different egg chambers. We observe a steady increase in Yp1:GFP in all oocytes (Egg chamber ages were estimated as in (C)). (C) A growth curve was generated based on the oocyte percent to estimate the age of the egg chambers to understand the timeline of yolk uptake and histone accumulation (see methods and Fig. S3A for correlation between egg chamber are and oocyte percent). (D) Stage 10 egg chamber expressing H2Av-mRFP during early nurse cell dumping. Note the flow of H2Av from the nurse cells into the oocyte. Squares indicate the region of the egg chamber quantified in E,G,K. (E) Quantification of average pixel intensities in the indicated regions of D normalized to the intensity of the follicle cell nuclei (NCC-Nurse cell cytoplasm; AO-Anterior oocyte cytoplasm; PO-posterior oocyte cytoplasm). Note the steady increase of H2Av in all three regions as it exits the nurse cell nuclei (F) A more advanced, stage 11 egg chamber during later stages of dumping. (G) Quantification of the H2Av intensity in different regions of the egg chamber shown in F over time. Note that H2Av declines in all regions at these later stages. (H-K) Changes to the normalized H2Av intensities in various parts of 8 independent egg chambers of various ages. Each color corresponds to the same egg chamber in all panels. Egg chamber ages were estimated from the standard growth curve in C based on the percent of egg chamber area occupied by the oocyte at t0. Together these data are consistent with H2Av being lost from nurse cell nuclei and flowing gradually posteriorly into the oocyte. (H) The total integrated nurse nuclear intensities represent the total amount of H2Av in the nurse cell nuclei over time. These intensities show a consistent decline over the course of nurse cell dumping indicating that H2Av is being lost from nurse cell nuclei. (I)The mean cytoplasmic intensity of the nurse cells indicate an initial increase followed by a decline in H2Av nurse cell cytoplasmic concentration. (J), The intensity in the anterior oocyte shows an initial dramatic increase followed by a slight decline (K), The intensity in the posterior oocyte is initially flat and increases only later during dumping. The accumulation is delayed compared to the anterior oocyte in J indicating an overall posterior flow. Images in (A D, F) were processed for presentation using background subtraction, gaussian filter and median filters in Fiji.

790 Movie 1 Fly restraint in Bellymount-PT mount kept on the bench for about 16 hours can lay eggs and stay
791 active.
792 Movie 2 Zoomed-out view of a mount kept at room temperature showing multiple females kept on bench
793 for about 16 hours.
794 Movie 3 A fly that survived 16 hours of imaging is still active and eggs deposited during the imaging period
795 are visible in the mount.
796 Movie 4 View through z stacks across stage 6 egg chamber imaged on the multiphoton microscope for a
797 single time frame (Fig. 2C).
798 Movie 5 3D reconstruction of two early egg chambers from Fig. 2C, 3D surface with H2Av-mRFP signal
799 Movie 6 3D reconstruction of two early egg chambers from Fig. 2C, 3D surface without H2Av-mRFP
800 signal
801 Movie 7 Tracking multiple egg chambers for 14 h through Bellymount-PT(scalebar = 100µm).
802 Movie 8 Tracking a stage 10 egg chamber through nurse cell dumping and dorsal appendage formation
803 during (scalebar = 50µm).
804 Movie 9 Tracking a young pre-vitellogeneic egg chamber (scalebar = 25µm)
805 Movie 10 Tracking egg chamber during active vitellogeneic stage (scalebar = 25µm)
806 Movie 11 Yp1 uptake by an stage 8 egg chamber
807 Movie 12 Early stages of nurse cell dumping and transfer of H2Av-mRFP
808 Movie 13 Late stage nurse cell dumping and transfer of H2Av-mRFP
809 Movie 14 Proof of principle movie to show that we can visualize border cell, however speed of the border
810 cell migration is much slower
811
812
813
814
815
816
817
818
819
820
821
822
823

Fig. S1

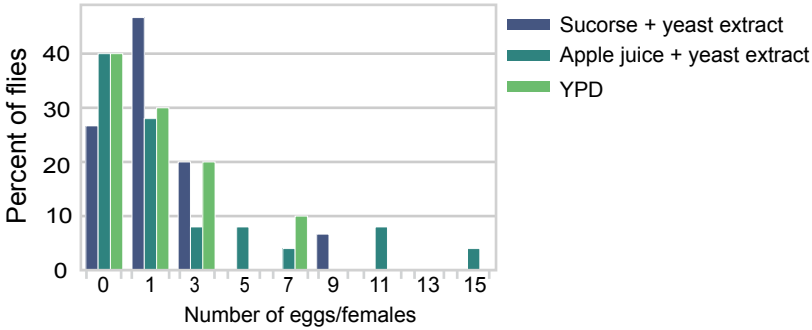
Percent of flies
40
30
20
10
0
0
1
3
5
7
9
11
13
15
Number of eggs/females
Sucorse + yeast extract
Apple juice + yeast extract
YPD

Supplemental Figures.

Fig.S1. Different liquid foods were tested for their ability to support oogenesis during long term imaging We tested combination of glucose and protein diet in a liquid media to ensure the flies are hydrated, and they are not deprived of proteins diet, as that could affect their egg production. We used 10% sucrose water with yeast extract (n=15), apple juice extract with yeast extract as apple juice is used in egg collection protocols (n=25) and yeast extract peptone dextrose media (n=10). We added a few grains of active yeast into these solutions. Though we did not observe any significant difference in the average eggs laid by females fed with these diets ($p<0.05$) when we looked at the frequency of eggs laid we found that females laid maximum number of eggs when fed with apple juice with yeast extract.

Fig. S2

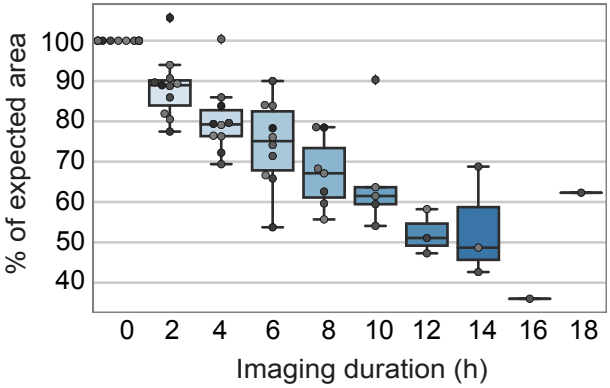
% of expected area
100
90
80
70
60
50
40
0
2
4
6
8
10
12
14
16
18
Imaging duration (h)

Fig.S2. Box plots of the percent of expected area each egg chamber had achieved by the given hour of imaging. Note that egg chamber growth is slowed in the imaged females compared to the expected values derived from fixed samples (Figure 3B) (n=31, egg chambers staged from 4-8).

Fig. S3

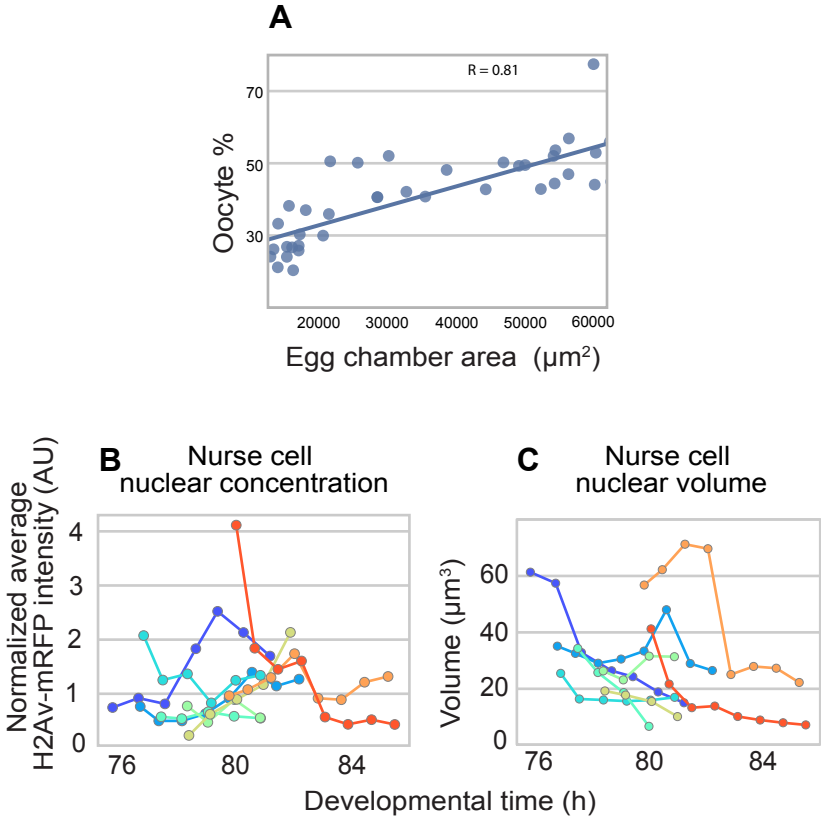
A
R = 0.81
Oocyte %
70
50
30
20000
30000
40000
50000
60000
Egg chamber area (μm²)
B
Nurse cell
nuclear concentration
Normalized average
H2Av-mRFP intensity (AU)
4
3
2
1
0
76
80
84
C
Nurse cell
nuclear volume
Volume (μm³)
60
40
20
0
76
80
84
Developmental time (h)

892 Fig.S3 (A) Correlation plot of the oocyte percent against the overall egg chamber area (n=44). We used
893 whole egg chamber size to measure the growth rates (Figure 3). However, we relied on oocyte percent to
894 stage the events that occur during vitellogenesis and dumping (Figure 4). (B and C) Are additional
895 quantifications of the egg chambers in Fig.4 D-K. (B)The H2Av-mRFP average pixel intensity
896 (concentration) of H2Av-mRFP remains relatively constant, or slightly increasing during early nurse cell
897 dumping. (C) Conversely, the total nurse cell nuclear volume falls steadily throughout dumping. This results
898 in the steady decrease in total H2Av-mRFP signal observed in Fig. 4H.
899
900
901
902
903
904
905
906
907
908
909
910
911
912
913
914
915
916
917
918
919
920
921
922
923
924
925

Fig. S4

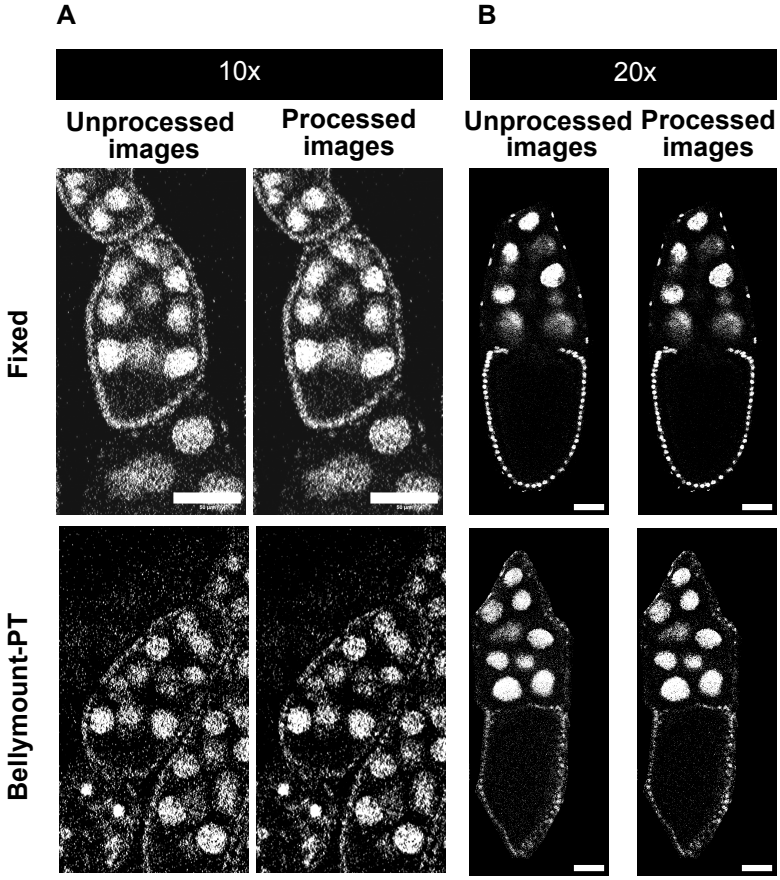
A
B
10x
20x
Unprocessed images
Processed images
Unprocessed images
Processed images
Fixed
Bellymount-PT

Fig.S4. Comparison of unprocessed and processed images for presentation in figures. We used lower degree of filtering to clear the noise from the images. Note that the images used for analysis were not processed. We used commonly used processing protocol involving brightness and contrast adjustments, background subtraction, gaussian filter and median filter. (A) is an imaged captured on 10x objective while (B) from a 20x objective.

Table S1: Frequency distribution and developmental duration of individual chambers from stage 2-14, and the total cumulative duration of oogenesis to each stage.

Stages	Egg chambers	Frequency	Duration /stage (h)	Total cumulative duration of oogenesis' to each stage (h)
2	23	9.8291	8.4854	8.4854
3	29	12.3932	10.6990	19.1845
4	31	13.2479	11.4369	30.6214
5	23	9.8291	8.4854	39.1068
6	31	13.2479	11.4369	50.5437
7	26	11.1111	9.5922	60.1359
8	18	7.6923	6.6408	66.7767
9	16	6.8376	5.9029	72.6796
10	11	4.7009	4.0583	76.7379
11	3	1.2821	1.1068	77.8447
12	9	3.8462	3.3204	81.1650
13	2	0.8547	0.7379	81.9029
14	12	5.1282	4.4272	86.3301

10 Supp. Table 2: Information related to microscopy and image processing for all images in this paper

11

Figure	Microscope: Mode	Objective	Fluorophores: Laser	Pixel size: Pixel time:	Imaging interval	Background subtraction: Gaussian blur: Median blur
1F	LSM980 Airyscan MPLX CO-8Y	Plan-Apochromat 20x, 0.8M27.	H2Av-mRFP 561 nm, 1%	0.171 x 0.171 x 3 µm 0.32 µs	Fixed samples	50 pixel radius: 0.5 pixel radius:1pixel radius: Images were compiled from individual females from different biological experiments
1G	LSM980 Airyscan MPLX CO-8Y	Plan-Apochromat 20x, 0.8M27.	H2Av-mRFP 561 nm, 0.3%	0.171 x 0.171 x 3 µm 0.32 µs	Single time frame live fly	
2C-D	Olympus FVMPE-RV Multiphoton system	25x XLPLN25×WMP2, NA 1.05 531	Moesin-GFP, 920 nm H2Av-mRFP, 1040 nm	0.497 x 0. 497 x 3 µm 0.012 s	Bellymount-PT sample acquired at a single time frame	50 pixel radius: 0.5 pixel radius:1pixel radius. E in E' were not subjected to processing as 3D reconstructions were carried for raw images.
2F	LSM980 Airyscan MPLX CO-8Y	Fluar 10x/0.50 M27 Air objective	H2Av-mRFP 561 nm, 0.3%	0.274 x 0.274 x 5 µm 0.34 µs	Fixed sample	50 pixel radius: 0.5 pixel radius:1pixel radius
2G					Bellymount-PT samples imaged every 2h once	50 pixel radius: 0.5 pixel radius:1pixel radius: Same egg chamber imaged in a given panel
2H						
3F	LSM980 Airyscan	Fluar 10x/0.50 M27 Air objective	H2Av-mRFP 561 nm, 0.3%	0.274 x 0.274 x 5 µm 0.34 µs	Bellymount-PT samples imaged every 2h once	50 pixel radius: 0.5 pixels:1pixel: Same egg chamber from an individual female imaged in each panel
3H						

	MPLX CO-8Y					
4A	LSM980 Airyscan MPLX CO-8Y	Plan-Apochromat 20x, 0.8M27.	Yp1-sfGFP 488nm, 0.2% H2Av-Endo-mCherry 561 nm. 0.3%	0.149 x 0.149 x 4 µm 0.56 µs	Bellymount-PT samples imaged every hour	50 pixel radius: 0.5 pixels:1pixel: Same egg chamber from an individual female is represented in a given panel
4D			H2Av-mRFP: 561 nm, 0.3%	0.171 x 0.171 x 3 µm 0.32 µs	Bellymount-PT samples imaged every ~10 min	
4F						
Movie1	digital USB-pluggable 60x-250x Digital microscope	NA	Bright field	NA	Acquired manually	These images rotated and cropped to set to desired orientation after acquiring.
Movie2						
Movie3						
Movie4	Olympus FVMPE-RV Multiphoton system	Same image presented in Fig. 2C shown in through the z sections				
Movie5		Two egg chambers represented in Fig.2D were 3D reconstructed using H2Av-mRFP signal for germline cell and H2Av-mRFP was used for the surface reconstruction of the whole egg chambers using Arivis 4D vision program. 2D images of the reconstructions are shown in Fig. 2E and E’				
Movie6						
Movie7	LSM980 Airyscan MPLX CO-8Y	Zoomed out view of egg chambers in the imaging field of view represented in Fig.2G. The movie has all the time frames captured for 16 hours. Entire time frames were processed as described in the Fig. 2G and selective time frames were presented. In the movie and the figures represent the midsection view of the egg chambers				
Movie8		Midsection of an individual egg chamber starting at stage 10 at the beginning of the imaging. The movie was processed as described for Fig. 2H and selected time frames are represented in the figure, while the movie has captured for 10 hours.				

Movie9		Midsection of a previtellogenic egg chamber starting at stage 7 at the beginning of the imaging. The movie was processed as described for Fig. 3F and selected time frames are represented in the figure, while the movie has captured for 8 hours.				
Movie10		Midsection of a vitellogenic egg chamber starting at stage 10 at the beginning of the imaging. The movie was processed as described for Fig. 3H and selected time frames are represented in the figure, while the movie has captured for 12 hours.				
Movie11		Midsection of stage 8 egg chamber at initial stages of yolk uptake capture for 4h, the image was processed as described in Fig. 4A.Images were acquired at every hour.				
Movie12		In figure 4D the images were acquired every 10min to capture histone loading. Defined ROI were measured for H2Av-mRFP fluorescent intensities for only every fifth time frame from the raw files, while represented figures and movie was process as described for Fig 4D.				
Movie13		In figure 4E the images were acquired every 10 min to capture histone loading. Defined ROI were measured for H2Av-mRFP fluorescent intensities for only every fifth time frame from the raw files similar to Movie 12, while represented figures and movie was process as described for Fig 4F.				
Movie14		Plan-Apochromat 20x, 0.8M27	H2Av-mRFP: 561 nm, 0.3%	0.171 x 0.171 x 3 µm 0.32 µs	Bellymount-PT samples imaged every ~11 min for about 3 hours	100 pixel radius: 2 pixel radius:2 pixel radius
Movie15					Bellymount-PT samples imaged every ~10 min for about 5 hours	100 pixel radius: 2 pixel radius:2 pixel radius

Movie16					Bellymount-PT samples imaged every ~10 min for 6 hours	100 pixel radius: 2 pixel radius:2 pixel radius: These egg chambers were from the same sample presented in Fig.4 D, and movie 12. But processed differently to visualize follicle cell layer better to appreciate the egg chamber rotation in vivo.